Classification: Physical Sciences, Applied Physical Sciences

Title: Reconfigurable microbots folded from simple colloidal chains

Authors: Tao Yang[1], Brennan Sprinkle[2], Yang Guo[1], Jun Qian[3], Daoben Hua[3], Aleksandar Donev[2], David W.M. Marr[1]*, and Ning Wu[1]*

Author affiliation: [1]Department of Chemical and Biological Engineering, Colorado School of Mines, Golden, Colorado, USA 80401

[2]Courant Institute of Mathematical Sciences, New York University, New York, New York, USA 10012.

[3]State Key Laboratory of Radiation Medicine and Protection, School for Radiological and Interdisciplinary Sciences (RAD–X), Soochow University, Suzhou, China 215123.

Corresponding author: Ning Wu and David W. M. Marr

Department of Chemical & Biological Engineering

Colorado School of Mines

1500 Illinois St, Golden, CO 80401

Email: ningwu@mines.edu and dmarr@mines.edu

Keywords: Colloidal chain, magnetic field assembly, folding, propulsion

Abstract

To overcome the reversible nature of low-Reynolds number flow, a variety of biomimetic micro-robotic propulsion schemes and devices capable of rapid transport have been developed. However, these approaches have been typically optimized for a specific function or environment and do not have the flexibility that many real organisms exhibit to thrive in complex microenvironments. Here, inspired by adaptable microbes and using a combination of experiment and simulation, we demonstrate that one-dimensional colloidal chains can fold into geometrically complex morphologies including helices, plectonemes, lassos, and coils and translate via multiple mechanisms that can be varied with applied magnetic field. With chains of multi-block asymmetry, the propulsion mode can be switched from bulk to surface-enabled, mimicking the swimming of microorganisms such as flagella-rotating bacteria and tail-whipping sperm and the surface-enabled motion of arching and stretching inchworms and sidewinding snakes. We also demonstrate that reconfigurability enables navigation through three dimensional and narrow channels simulating capillary blood vessels. Our results show that flexible microdevices based on simple chains can transform both shape and motility under varying magnetic fields, a capability we expect will be particularly beneficial in complex *in vivo* microenvironments.

Significance Statement

Most microscale swimmers and some larger animals utilize long filaments or slender bodies for propulsion, since one-dimensional chains are the simplest structure that can be bent, twisted, braided, or folded into a wide range of geometrically or topologically complex morphologies. Inspired by this, here we fabricate flexible magnetic colloidal chains that can enable significant freedom of morphology change and motion using an applied precessing magnetic field. As the result of their reconfigurability, these systems can switch propulsion mode from free swimming to surface-enabled translation, enabling navigation through complex 3D environments such as channels that mimic arteries, veins, and capillaries. The demonstrated shape change and adaptability are ubiquitous in natural systems and are necessary for microbot navigation in complex environments.

Propulsion at the microscale is challenging due to the reversible nature of low-Reynolds flow(1). Despite this, microorganisms such as prokaryotes and sperm are able to swim in complicated biological environments by waving their flagella or cilia to drive processes essential for life ranging from nutrient transport to pathogen clearance. To control their motion, these biological motors have evolved to be flexible, adaptive, and polymorphic. For example, the flagellum morphology of the photosynthetic bacterium *Rhodobacter sphaeroides* can shift from a helix to an in-plane coil to slow down and reorient the cell (2). *E. coli*, when sensing nutrients, can change the rotating direction of flagella from counter clockwise to clockwise, where the flagellum bundle falls apart (3). And the flagellum of an entrapped *S. putrefaciens* bacterium can adapt a radical change into a spiral-like shape that wraps around the cell body to generate a large force to escape (4). Flexibility is also used by animals outside of the low-Reynolds number regime. Snakes, for example, take advantage of underlying surfaces to achieve multiple movements such as concertina, serpentine, sidewinding, and rectilinear locomotion (5).

Although significant progress has been made in mimicking natural swimmers by synthetic microbots (6-12), most of them have been fabricated with rigid structure, preventing shape change and adaptation. Recently, reconfigurable artificial swimmers based on millimeter-scale magnetic hydrogel nanocomposites or three-dimensional (3D) printing have been fabricated (13-17). With preprogrammed ferromagnetic domain distributions and changing external magnetic field, such systems can deform into 3D architectures (16) to roll, jump, swim, crawl, and transport cargo under command (15). However, their sizes are large compared with their biological counterparts, preventing *in situ* applications. Other types of shape-morphing micromachines have also been reported based on the origami principle and spatial patterning of

heterogeneous materials (18-21). They, however, have either been limited to one type of transformation or have relied on sophisticated fabrication techniques (20, 21).

For propulsion most biological swimmers utilize one-dimensional (1D) elastic filaments, the simplest structure that can be bent, twisted, braided, or folded into a wide range of geometrically or topologically complex morphologies. Indeed, flexible chains such as polypeptides and polynucleotides are ubiquitous in biological systems. Although they have relatively simple backbones, by virtue of site-specific interactions between rather limited sets of subunits along the chains, they can fold into proteins and DNA molecules with well-defined 3D structures of exquisite complexity and functionality. Inspired by the polymorphic nature of linear chains, we extend our previous work on the assembly of magnetic wheel-based translating microbots (22, 23) to incorporate flexible linkages between component colloidal building blocks to fabricate magnetic colloidal polymers that enable significantly greater freedom of motion. We then demonstrate that magnetic chain microbots can readily undergo shape transformation with a precessing magnetic field change. These systems, both homogeneous and heterogeneous suggestive of cargo transport, can switch propulsion modes and, as a result of their flexibility and reconfigurability, they can adapt within complicated three-dimensional environments such as confined channels.

Results and Discussion

Fabrication of semi-flexible magnetic chains   Magnetic chains were fabricated by chemically linking superparamagnetic particles (Dynabead Myone™, diameter $2a = 1.05$ μm, density $\rho = 1.8$ g/cm^3) with 4-arm polyethyene glycol (PEG) maleimide (see SI Appendix, Sec. 1, Fig. S1, and Fig. S2). In this, available carboxylic acid groups on the particle surface were converted into thiols via carbodiimide chemistry. Under a 1D direct-current (DC) magnetic field,

surface modified particles suspended in dimethyl sulfoxide (DMSO) chain together due to dipolar attractions. The thiol functional groups on the particle surfaces then react with maleimides in the PEG linkers via a Michael addition reaction; as a result, chemically stable but flexible linkages form between neighboring particles (24). With this approach, the maximum chain length L is ~ 60 µm. The chain bending modulus $\kappa_{bend} = EI$ (where E is the Young's modulus and $I = \pi a^4/4$ is the moment of inertia) can be determined by bending an initially straight chain into a U-shape along the orthogonal direction (SI Appendix, Fig. S3). Based on the measured separation between two legs of the U-shaped chain (25, 26), we have determined κ_{bend} =10^{-24}-10^{-26} J·m, tunable by fabrication field strength and degrees of thiol functionalization (SI Appendix, Fig. S2E). By comparing the spring constant k_0 of a single PEG linker and the overall spring constant of the colloidal chains k_{tot} and assuming that the PEG linkers are springs connected in parallel between particles, we have estimated that the number of PEG linkers between neighboring particles ranges from 2 to 160 (SI Appendix, Sec. 4 and Fig. S5). In this work, we focus on semi-flexible chains for which the ratio of the chain contour length L to the persistent length L_p ($L_p = k_{bend}/k_B T$, where $k_B T$ is the thermal energy) is of order 1 to 10. This ratio is comparable with those found in real flagella (27) and other synthetic magnetic chains (28-30), indicating similar flexibilities. While chain diameters are 50 times larger than those of flagella with a corresponding moment of inertia 10^7 times larger, an effective Young's modulus 10^7 times smaller leads to a bending modulus of similar magnitude. Comparable flexibilities enable chains to fold and propel similarly to their smaller-scale natural counterparts. All the experiments described here were performed by dispersing fabricated chains in DMSO (viscosity = 1.996 cP) to prevent sticking. In deionized water, we observed that chains adhered to glass surfaces quickly with apparent electrostatic attractions and zeta potential reduction due to the

conversion of carboxylic acid surface functional groups into thiols and dissociation of nitrogen

atoms from linker maleimide groups. With observed propulsion velocities of 1 – 10 μm/s, we

calculate Reynolds numbers of order $10^{-4} - 10^{-5}$, well within the Stokes regime. Note that, given

the smooth nature and low surface roughness (~10 nm) of glass slides, the impact of surface

topography on chain propulsion can be neglected.

Folding and propulsion of chains under precessing magnetic fields   We and others have

shown that a flexible magnetic chains can be folded into "U" and "S" shapes under 1D fields (25,

26, 31, 32) or coiled into "lassos" under 2D rotating magnetic field (29, 33, 34). Theories have

predicted that spiral or helical shapes are possible under 3D precessing fields (35, 36). No

experimental work, however, has so far demonstrated the folding of colloidal chains into helices

primarily due to the challenge in making chains of sufficient flexibility. As shown in SI

Appendix Fig. S4, we apply a precessing magnetic field, i.e., the superposition of a DC field

along the x-axis and a circularly rotating field in the y-z plane

$$\mathbf{B} = B_x\hat{\mathbf{x}} + B_{yz} sin(\omega_M t)\hat{\mathbf{y}} + B_{yz} cos(\omega_M t)\hat{\mathbf{z}}, \tag{1}$$

where ω_M is the angular frequency of the applied field, B_x and B_{yz} are the magnetic flux

densities. $\hat{\mathbf{x}}$ and $\hat{\mathbf{y}}$ are in-plane unit vectors parallel to the substrate and $\hat{\mathbf{z}}$ is perpendicular to the

substrate. The unit vector $\hat{\mathbf{B}} = (cos\beta,\ sin\beta\ sin(\omega_M t),\ sin\beta\ cos(\omega_M t))$ points towards the

magnetic field direction, where $\beta = \tan^{-1}(B_{yz}/B_x)$ is the so-called cone angle. This specific

field orientation was chosen to aid visualization of chain morphologies under optical

microscopy. By tuning both field strength and cone angle, we have been able to fold individual

chains into helices (Fig. 1A and SI Appendix, Movie 1A). In this case, the two ends of an

initially straight chain coil with opposite chirality and rotate due to the rotating field in the y-z

plane. Subsequent chain coiling then propagates towards the center and one of the chiralities

"wins", potentially due to small perturbation during folding or some mild heterogeneity in chain flexibility, and a stable helix is formed.

Qualitatively, the formation of a helix results from the competition between the x-DC field and y-z rotating field. If the rotating field B_{xy} is strong, the chain folds into a closed-loop lasso in the y-z plane while the chain will be stretched into a rigid rod if the DC field B_x is strong. We have found that a helix only formed within a narrow regime of the full phase diagram (Fig. 1B) where the cone angle is slightly larger than the magic angle $\beta = acos\sqrt{1/3} = 54.7°$ for which the time-averaged dipolar magnetic interactions nearly vanish, consistent with theoretical predictions (35, 36). Moreover, as shown in Fig. 1C, the helical morphology, characterized by the ratio of pitch to perimeter, $p/\pi D$, can also be conveniently controlled by the so-called magnetoelastic parameter (35) $M_n = \pi a^2 \chi^2 B^2 L^2 (1 - 3\cos^2\beta)/36 k_{bend}\mu_0$, where μ_0 is the permeability of free space, χ is the magnetic susceptibility of the particle, and $B = \sqrt{B_x^2 + B_{yz}^2}$. Compared with prefabricated and rigid microhelices (7-9), our chains are able to fold into flexible helices with the corresponding helix angles $\theta = \cot^{-1}(p/\pi D)$ ranging from ~60° to 90° solely by manipulating external magnetic field conditions.

Helices, once formed, demonstrated unique 3D propulsion capability due to their intrinsic broken symmetry under the same precessing field. Also shown in SI Appendix, Movie 2A, the helix propels along both x- and y-axes. Its motion in the y-axis is due to its interaction with the wall and a rotation-translation coupling arising from the circularly rotating y-z field, similar to the rolling of both lassos and rods (SI Appendix, Movie 2B and 2C). The translation of a helix along the x-axis is, however, due to its helical shape. Based on resistive force theory (37-39), the propulsion velocity V and applied torque Γ on a helix are related to the applied force $\mathbf{F}$ and its angular frequency ω via the matrix

$$\begin{pmatrix} \mathbf{V} \\ \boldsymbol{\Gamma} \end{pmatrix} = \begin{pmatrix} A & -B \\ B & C \end{pmatrix} \begin{pmatrix} \mathbf{F} \\ \boldsymbol{\omega} \end{pmatrix}, \tag{2}$$

where the constants A, B, and C are

$$A = \frac{\sin\theta}{N\pi D(\zeta_\parallel \cos^2\theta + \zeta_\perp \sin^2\theta)}$$

$$B = \frac{D(\zeta_\parallel - \zeta_\perp)\tan\theta}{2(\zeta_\parallel + \zeta_\perp \tan^2\theta)}$$

$$C = \frac{N\pi D^3 \zeta_\perp \zeta_\parallel}{4\sin\theta\,(\zeta_\parallel \cos^2\theta + \zeta_\perp \sin^2\theta)}, \tag{3}$$

and N is the number of turns in the helix, with $\tan\theta = \pi D/p$. Here $\xi_\perp$ and $\xi_\parallel$ are the viscous

drag coefficients perpendicular and parallel to the helix segment, respectively (40).

$$\zeta_\perp = \frac{4\pi\eta}{ln\left[\frac{0.18\pi D}{a\sin\theta}\right] + 0.5} \qquad\qquad \zeta_\parallel = \frac{2\pi\eta}{ln\left[\frac{0.18\pi D}{a\sin\theta}\right]}. \tag{4}$$

Since the helix is actuated under a uniform magnetic field, there is no magnetophoretic force and

the chain is force free, $\mathbf{F}=0$, and Eqn. (2) can then be simplified as

$$\frac{V}{\omega D} = \frac{(1-\gamma_k)p}{2\pi D[\gamma_k(p/\pi D)^2 + 1]}, \tag{5}$$

where $\gamma_k = \xi_\parallel/\xi_\perp$. This scaling matches well with our experimental data of helical motion along

the x-direction (Fig. 1D). The highest propulsion coefficient that can be achieved in our chains is

$V/\omega D \sim 0.08$, slightly smaller than rigid helices (9) but comparable with that of *E. coli* (~ 0.1

with $V \sim 25$ µm/s, $\omega \sim 628$ rad/s, and $D \sim 0.4$ µm) (41).

Numerical simulation of chain folding and propulsion   To further understand the response

of colloidal chains under different magnetic fields, we use numerical simulation where the

colloidal chain is modeled as linked spherical beads of radius a. In the model, the magnetic force

on bead i due to the interaction with neighboring bead j is (42)

$$\boldsymbol{F}_{i,j}^{\mathrm{mag}} = \frac{F_0}{(r_{i,j}/a)^4} \left(2(\hat{\boldsymbol{m}} \cdot \hat{\boldsymbol{r}}_{i,j}) \bar{\hat{\boldsymbol{m}}} - \left(5(\hat{\boldsymbol{m}} \cdot \hat{\boldsymbol{r}}_{i,j})^2 - 1 \right) \hat{\boldsymbol{r}}_{i,j} \right) , \qquad (6)$$

where $F_0 = 3\mu_0 \, m_0^2 / 4\,\pi a^4$, $m_0 = 4\pi a^3 \chi \, B_0 / 3\,\mu_0$, and $\hat{\boldsymbol{m}} = \boldsymbol{m}/m_0$ is the scaled magnetic moment of a bead; magnetic interactions between non-neighboring beads are neglected. Since the beads are superparamagnetic, we assume that the direction of the induced magnetic moment aligns instantaneously with the direction of the applied field $B(t)$. We resolve the time-dependence of the magnetic field instead of averaging the magnetic interactions over one period of oscillation as done in prior theoretical work (36). This requires that the time step size be much smaller than the period of the AC component of the applied field. Using at least 20 time steps per period resolved the time dependence of the magnetic forces adequately.

The chain elasticity is modeled using a penalized (slightly extensible) discrete version of the Kirchhoff continuum model of an inextensible rod, following prior work by others (43, 44), and explained in more detail in the SI. We obtain the bending modulus κ_{bend} from the response of a straight chain to a perpendicular DC field, as we will elaborate later. The twist modulus κ_{twist} cannot be independently measured, so we have selected its value to closely reproduce the dynamics of helix formation in the experiments.

We use the fast, minimally resolved Brownian dynamics method presented in (45) to simulate the dynamics of folding and propulsion of colloidal chains. This method is based off of Stokesian dynamics (46), but omits stresslets and only uses the Rotne–Prager–Blake (47, 48) tensor to compute the translational and rotational hydrodynamic mobility between particles of radius a suspended above a bottom wall. We include near-field lubrication corrections to the hydrodynamics following Brady *et al.* (46) for both neighboring pairs of particles along the magnetic chain and between individual particles and the bottom wall. These lubrication corrections improve the accuracy of the hydrodynamic model. Accounting for lubrication also

allows us to use a more short-ranged and stiff steric repulsion to impose nearly strict

inextensibility of the chain, without incurring a severe restriction on the time step size, primarily

because of the strong reduction of the mutual mobility for nearly touching particles. Further

details of our simulation method are described in the SI Appendix, Sec. 3.

To validate our simulation method and obtain values for the bending modulus, we first

simulate the bending of a straight chain under an applied DC field in the direction orthogonal to

the initial chain alignment. As shown in SI Appendix Fig. S3 and Movie 3, a chain of 40 beads

gradually bends into U shape. The separation between two legs Δ depends on the field condition

and the bending modulus of the chain. By substituting the properties of Dynabeads and the exact

experimental conditions, and tuning the bending modulus $\kappa_{bend} = \kappa_{bend}^{const} = 2.0 \times 10^{-24}$ J·m,

we are able to match the simulated Δ with experiments. We note that this value of κ_{bend} is also

consistent with what we measured in experiments. The time scale of the chain folding in

simulation is also in fair agreement with experiments. After obtaining the bending modulus, we

simulate the folding of a 60-mer chain under a 3D precessing field (SI Appendix, Movie 1B) and

the snapshots are shown in Fig. 1A. The chain morphologies as a function of time match well

with our experiments, validating our simulation method. For this simulation we took the bending

modulus to be variable along the length of the chain such that $k_{bend}(s) = \kappa_{bend}^{const}(3 + 2s/L)/5$

where s is the arc length. This variable form of $k_{bend}(s)$ was chosen *ad hoc* to give the chain

some flexural heterogeneity and its actual form is not critical. This heterogeneity, however, was

important to be included in the simulations of swimming helices as perfectly homogeneous

chains typically develop a kink in their chirality in the middle of the chain, thus exhibiting no

preferred swimming direction. In experiments however, the development of chain chirality is

eventually dominated from one of the two ends, likely due to mild heterogeneity in the bending

modulus, which is unavoidable during the linking stage. For shorter chains such as 40mers however, an initial small perturbation of the chain configuration was enough to break the symmetry, without having to include flexibility heterogeneity (Fig. 2 and SI Appendix, Fig. S3, with simulation conditions summarized in SI Appendix, Table S2).

Sequential folding and motion of homogeneous chains

We note that the morphology of a folded chain depends on its initial configuration and the magnetic field conditions. Therefore, we are able to fold the chain sequentially along different pathways as shown in Fig. 2A (Config. 1-3) where a linear chain is pre-aligned with the DC field in the x-direction. The addition of an AC field along the y-direction induces oscillation in the same direction. Further superposition of an AC field in the z-direction, i.e., a 3D precessing field, eventually folds the chain into a helix, as we have previously demonstrated. On the other hand, the U- and S-shaped chains in Figs. 2B and 2C form depending on the initial chain configurations along the x-direction. If both ends of the chain initially curve inwards slightly, the chain will transform into a U-shaped chain when a DC field is applied in the y-direction. In contrast, if one end curves inwards and the other end curves outwards slightly, the chain forms an S shape when the y-DC field is applied, as shown in simulations (31). Further application of the 3D precessing field allows the two parallel legs of the U-shaped chain to twist together, forming a plectoneme (Config. 8), while the S-shaped chain folds into a coiled configuration (Config. 9). These chain morphologies and folding pathways are also reproduced in our numerical simulations by using the same experimental conditions (Fig. 2 with simulation conditions summarized in SI Appendix, Table S2).

Chain morphology determines whether a chain exhibits net propulsion or not. Under 2D fields, no net translation is observed for oscillating linear and "S"-shaped chains since their fore-

aft symmetries are not broken. The "U"-shaped chain, however, is asymmetric. Its two free legs oscillate with higher amplitude than its bent head and, as a result, it translates towards the tail (SI Appendix, Movie 4). Under 3D precessing fields on the other hand, both helices and plectonemes exhibit net propulsion perpendicular to their rotating directions, depending on their chirality (SI Appendix, Movie 4). The highly coiled chain in Config. 9 cannot move because its overall shape is approximately isotropic.

Multimodal propulsion of heterogeneous chains

Unlike homonuclear polymers, our colloidal chains, even when fabricated with monodisperse magnetic colloids, occasionally exhibit noticeable bending stiffness heterogeneities along the chain. For example, Fig. 3A shows a chain with one malformed point defect highlighted by the red arrows, where the tail is curved. This breaks the fore-aft symmetry and allows the tail to rotate as a rigid helix under a 3D precessing field (SI Appendix, Movie 5A). As a result, the chain moves with its rigid head leading along the x-axis, with minimal rolling in the orthogonal y-direction. More controlled heterogeneous diblock or triblock chains can be fabricated by sequentially attaching larger particles to the ends of single block chains composed of smaller particles. Such structures could also be investigated within the context of cargo transport where the rigid head, even if inert, is to be moved and delivered to a desired target. Fig. 3B shows a long and flexible chain linked to a large 2.7 μm magnetic bead. Under the same field, its helical motion mimics a rotating bacteria flagellum (SI Appendix, Movie 5B). A comparison between these two types of chains sheds light on their differences. The tail in Fig. 3A retains its shape during rotation and behaves like a rigid helix. As a result, its axial swimming velocity is considerably larger than lateral rolling. On the other hand, the chain in Fig. 3B is so flexible that one can see the propagation of waves along the chain. Interestingly, the chain

flexibility lowers its axial velocity. Significant rolling along the orthogonal direction due to the nearby wall is observed. For both cases, we are able to reverse the propulsion direction by switching the rotation direction.

More complicated bio-inspired propulsion modes, reminiscent of animal propulsion not necessarily relying on low Reynolds number flow can be created by taking further advantage of the nearby substrate. For example, a diblock chain can undergo undulatory beating (Fig. 3C and SI Appendix, Movie 6) on a substrate in a 2D field of $\mathbf{B} = B_x\hat{\mathbf{x}} + B_y\,sin(\omega_M t)\hat{\mathbf{y}}$, mimicking the planar beating of spermatozoa. We note that our diblock chains swim with the larger magnetic beads leading. The bending wave propagates from its larger head towards the free end, which is in the opposite direction from chains that are attached to red blood cells (6). When a 2D magnetic field is applied in the x-z plane, $\mathbf{B} = B_x\hat{\mathbf{x}} + B_z\,cos(\omega_M t)\hat{\mathbf{z}}$, a triblock chain undergoes inchworm-like motion (Fig. 3D and SI Appendix, Movie 7). The chain bends into a tilted asymmetric arch on the substrate because of the DC field along the z-direction and some chain heterogeneity. As one end is closer to the substrate than the other end, the difference in hydrodynamic drag causes a net propulsion via cyclic bending and stretching. When a 3D field such as $\mathbf{B} = B_x\hat{\mathbf{x}} + B_y\,sin(\omega_M t)\hat{\mathbf{y}} + B_z\hat{\mathbf{z}}$ is applied, a diblock chain also tends to curve into an arch. With the middle part of its body lifting up, the undulatory field in the y-direction propels it on the substrate like a sidewinding snake (Fig. 3E and SI Appendix, Movie 8).

Comparison of propulsion modes

We compare different propulsion modes reported previously in the literature with the propulsion mechanisms of our colloidal chains in Fig. 4. The radial axis of the polar plot represents the characteristic length D and the angle axis corresponds to the helix angle θ (defined in Fig. 1C). All 2D swimmers including undulating chains, rolling rods, and rotating lassos lie on

the radius axis since their helix angles are 90°. The propulsion coefficient is defined as $V/\omega D$, where D, the characteristic length, is chosen to be the diameter of the cross-section for a helix, lasso, and plectoneme. For 2D swimmers, D is twice the actuation amplitude as chosen in previous studies (37). We can see from Fig. 4 that the propulsion of 3D swimmers is overwhelmingly more efficient than their 2D counterparts. One exception is the microlasso previously reported by us (34) (the green square, $V/\omega D \sim 0.075$). As our chains are reconfigurable, we can readily switch the propulsion modes from 2D to 3D with the same length scale D but varying helix angles θ. For a homogeneous chain, the helical rotation (Config.7) is the most efficient 3D propulsion mode compared with the rotation of plectonemes and coils (Config. 8 and 9). From Eqn. (5), we see the that the maximum propulsion efficiency,

$(V/\omega D)_{max} = (1-\gamma_k)/4\sqrt{\gamma_k}$, occurs at the optimal helix angle θ=arctan ($\sqrt{\gamma_k}$). Thus the smaller

γ_k is, i.e. the larger the aspect ratio of helix length to single particle diameter is, the more efficient the propeller is. This is why high-aspect-ratio microswimmers like *E. coli* (Config. 15) or synthetic nanohelix (Config. 19) are more efficient than helical chains, which are primarily limited by the maximal chain length obtained to date.

Chain locomotion in straight and curved channels

To better mimic microorganisms in nature, artificial microswimmers must be able to adapt within complicated external environments. Most recently, Huang *et al*. demonstrated that soft magnetic hydrogel composites can fit into complicated 3D microchannels (17). Here, we show that our 1D semi-flexible magnetic chains navigate within different environments through transformation of both shapes and propulsion modes solely controlled by magnetic fields.

First, linear chains can pass through straight PDMS channels ranging from 7 to 20 μm in width and height ~ 10 μm. As shown in Fig. 5a, a chain of length $L = 21$ μm with a single point

defect underwent an in-plane undulatory motion, entered, and moved through a channel of 9 μm

wide (SI Appendix, Movie 9). As expected, the chain propulsion efficiency, characterized by the

ratio of chain velocity and the product of beating frequency and chain length $V/(f_M L)$, depends

on both beating frequency f_M and the channel width w. For a given channel, the efficiency first

increases with increasing frequency, or here equivalently the Sperm number, $S_p = \left(\frac{2\pi f_M \zeta_\perp L^4}{\kappa_{bend}}\right)^{\frac{1}{4}}$,

because chain motion becomes non-reciprocal in time. As frequency increases further, the chain

beating amplitude, shown in the red curve in Fig. 5B, becomes smaller and the efficiency drops

quickly. Therefore, the existence of an optimal efficiency results from the competition between

the bending force and the viscous force. When the channel width is large (e.g., w=12 μm), the

propulsion efficiency reaches the maximum when the Sperm number is approximately 3, the

same as a chain propelling in the bulk (6, 49-51). However, when the chain is confined within a

narrower channel, the Sperm number associated with maximum propulsion efficiency will be

shifted. This is because the channel width becomes smaller than the maximal chain beating

amplitude so that the chain propulsion is hindered by the channel walls. For all cases, the

optimum propulsion efficiency occurs at the frequency where the beating amplitude is

comparable to the channel width. In our work, the narrowest channel which our chain can

navigate is ~ 7 μm, comparable to the size of typical capillary blood vessels.

     Beyond straight channels at the same elevation, we can also achieve 3D propulsion in

both bulk fluid and curved channels. This is possible because chain configurations 10-12 allow

for propulsion modes that do not rely on the existence of nearby walls. For example, Fig. 5C and

SI Appendix Movie 10 show that a helical chain can overcome the gravitational force and

undergo directed 3D propulsion. To achieve this, we apply a 3D precessing field $\hat{\mathbf{B}} =$

$(\cos\alpha\cos\beta - \sin\alpha\sin\beta\cos(\omega_M t))\hat{\mathbf{x}} + \sin\beta\sin(\omega_M t)\hat{\mathbf{y}} + (\sin\alpha\cos\beta +$

$\cos\alpha\sin\beta\cos(\omega_M t))\hat{\mathbf{z}}$ and reorient the magnetic cone orientation angle α (SI Appendix, Fig. S4 inset), which allows us to control the direction of the helix propulsion. To demonstrate this, we fabricated a 3D curved PDMS channel (1.78 x 0.80 x 0.55 mm), as reconstructed from confocal microscopy images and labelled by green fluorescent dyes in Fig. 5D, by pouring the PDMS precursor around a thin curved polymer thread, followed by dissolving the polymer with solvent (SI Appendix, Sec. 1.4 and Sec. 1.5). The red trajectory in Fig. 5D and SI Appendix Movie 11 demonstrate chain navigation within this curved channel over the change of 500 μm in elevation and 2 mm in length. For most of the trajectory, we folded the chain into lassos which rolled along the channel wall quickly. Whenever the chain encountered steep slopes where the surface-enabled propulsion mode became ineffective, we altered the field condition to transform the lasso into a helix which allows for free swimming within the channel (white trajectory in Fig. 5D). This example demonstrates that a colloidal chain can navigate through a curved channel and against gravity by changing both chain morphology and propulsion modes with different field conditions mimicking the adaptation of propulsion mechanisms in different environments seen in biological swimmers.

Conclusions

We fabricated one-dimensional semi-flexible superparamagnetic colloidal chains and demonstrated that they can fold into a variety of two- and three-dimensional shapes including helices, plectonemes, lassos, and coils, under varying magnetic fields. Under similar fields, the folded chains can be tuned to move either by surface-enabled or by free swimming, allowing for 3D propulsion. We have shown that free swimming can be achieved to overcome limitations due to low Reynolds number fluid mechanics by breaking chain symmetry with heterogeneity in stiffness along a homonuclear chain or with multiple blocks. Other heterogeneous chains instead

take advantage of nearby surfaces and exhibit different propulsion modes that closely mimic arching and stretching inchworms and sidewinding snakes. The transformation between different chain morphologies and locomotion modes, solely controlled by external magnetic fields, enables these high-aspect ratio colloidal chains to navigate through complex 3D environments such as long and curved channels and narrow channels similar to capillary blood vessels.

Data availability

All experimental data discussed in the paper are available in the main text and SI Appendix. The codes used in this work are available publicly in the github repository

https://github.com/stochasticHydroTools/.

Author contributions

N.W. and DWM.M. conceived the idea and designed the project. T.Y., Y.G., and J.Q. performed the experiments. T.Y. performed the magnetic field actuation experiments; T.Y. and Y.G. designed and fabricated narrow and 3D microchannels; J.Q. and D.H. conceived and designed the surface conjugation chemistry. B.S. and A.D. developed the numerical simulation code. T.Y., B.S., A.D., DWM.M. and N.W. analyzed the experimental and simulation results and wrote the manuscript.

Competing interests

The authors declare no competing interests.

References

1. E. M. Purcell, life at low Reynolds number. *Am J Phys* **45**, 3-11 (1977).
2. J. P. Armitage, R. M. Macnab, Unidirectional, intermittent rotation of the flagellum of Rhodobacter sphaeroides. *J Bacteriol* **169**, 514-518 (1987).
3. H. C. Berg, D. A. Brown, Chemotaxis in Escherichia coli analysed by three-dimensional tracking. *Nature* **239**, 500-504 (1972).
4. M. J. Kuhn, F. K. Schmidt, B. Eckhardt, K. M. Thormann, Bacteria exploit a polymorphic instability of the flagellar filament to escape from traps. *P Natl Acad Sci USA* **114**, 6340-6345 (2017).
5. D. L. Hu, J. Nirody, T. Scott, M. J. Shelley, The mechanics of slithering locomotion. *P Natl Acad Sci USA* **106**, 10081-10085 (2009).
6. R. Dreyfus *et al.*, Microscopic artificial swimmers. *Nature* **437**, 862-865 (2005).
7. A. Ghosh, P. Fischer, Controlled Propulsion of Artificial Magnetic Nanostructured Propellers. *Nano Lett* **9**, 2243-2245 (2009).
8. L. Zhang *et al.*, Artificial bacterial flagella: Fabrication and magnetic control. *Appl Phys Lett* **94**, 064107 (2009).
9. S. Tottori *et al.*, Magnetic Helical Micromachines: Fabrication, Controlled Swimming, and Cargo Transport. *Adv Mater* **24**, 811-816 (2012).
10. W. Gao *et al.*, Bioinspired Helical Microswimmers Based on Vascular Plants. *Nano Lett* **14**, 305-310 (2014).
11. C. Peters *et al.*, Superparamagnetic Twist-Type Actuators with Shape-Independent Magnetic Properties and Surface Functionalization for Advanced Biomedical Applications. *Adv Funct Mater* **24**, 5269-5276 (2014).
12. B. Jang *et al.*, Undulatory Locomotion of Magnetic Multilink Nanoswimmers. *Nano Lett* **15**, 4829-4833 (2015).
13. H.-W. Huang, M. S. Sakar, A. J. Petruska, S. Pané, B. J. Nelson, Soft micromachines with programmable motility and morphology. *Nat Commun* **7**, 12263 (2016).
14. G. Z. Lum *et al.*, Shape-programmable magnetic soft matter. *P Natl Acad Sci USA* **113**, E6007-E6015 (2016).
15. W. Hu, G. Z. Lum, M. Mastrangeli, M. Sitti, Small-scale soft-bodied robot with multimodal locomotion. *Nature* **554**, 81-85 (2018).
16. Y. Kim, H. Yuk, R. Zhao, S. A. Chester, X. Zhao, Printing ferromagnetic domains for untethered fast-transforming soft materials. *Nature* **558**, 274-279 (2018).
17. H. W. Huang *et al.*, Adaptive locomotion of artificial microswimmers. *Science advances* **5**, eaau1532 (2019).
18. V. Magdanz, M. Guix, F. Hebenstreit, O. G. Schmidt, Dynamic Polymeric Microtubes for the Remote-Controlled Capture, Guidance, and Release of Sperm Cells. *Adv Mater* **28**, 4084-4089 (2016).
19. M. Z. Miskin *et al.*, Graphene-based bimorphs for micron-sized, autonomous origami machines. *P Natl Acad Sci USA* **115**, 466-470 (2018).

20. Y. Alapan, B. Yigit, O. Beker, A. F. Demirörs, M. Sitti, Shape-encoded dynamic assembly of mobile micromachines. *Nat Mater* **18**, 1244-1251 (2019).
21. D. Jin *et al.*, Four-dimensional direct laser writing of reconfigurable compound micromachines. *Mater Today* **32,** 19-25 (2019).
22. T. O. Tasci, P. S. Herson, K. B. Neeves, D. W. M. Marr, Surface-enabled propulsion and control of colloidal microwheels. *Nat Commun* **7**, 10225 (2016).
23. T. Yang *et al.*, Microwheels on Microroads: Enhanced Translation on Topographic Surfaces. *Science Robotics* **4**, eaaw9525 (2019).
24. T. Yang, D. W. M. Marr, N. Wu, Superparamagnetic colloidal chains prepared via Michael-addition. *Colloids Surf. A Physicochem. Eng. Asp.* **540**, 23-28 (2018).
25. C. Goubault *et al.*, Flexible magnetic filaments as micromechanical sensors. *Phys Rev Lett* **91**, 260802 (2003).
26. V. P. Shcherbakov, M. Winklhofer, Bending of magnetic filaments under a magnetic field. *Phys Rev E* **70**, 061803 (2004).
27. S. Trachtenberg, I. Hammel, The rigidity of bacterial flagellar filaments and its relation to filament polymorphism. *J Struct Biol* **109**, 18-27 (1992).
28. J. Byrom, P. Han, M. Savory, S. L. Biswal, Directing Assembly of DNA-Coated Colloids with Magnetic Fields To Generate Rigid, Semiflexible, and Flexible Chains. *Langmuir* **30**, 9045-9052 (2014).
29. S. Kuei, B. Garza, S. L. Biswal, From strings to coils: Rotational dynamics of DNA-linked colloidal chains. *Phys Rev Fluids* **2**, 104102 (2017).
30. J. Zhao, D. Du, S. L. Biswal, Nonlinear multimode buckling dynamics examined with semiflexible paramagnetic filaments. *Phys Rev E* **98**, 012602 (2018).
31. A. Cebers, Dynamics of a chain of magnetic particles connected with elastic linkers. *J Phys-Condens Mat* **15**, S1335-S1344 (2003).
32. A. Cebers, Flexible magnetic filaments. *Curr. Opin. Colloid Interface Sci.* **10**, 167-175 (2005).
33. A. Cebers, H. Kalis, Dynamics of superparamagnetic filaments with finite magnetic relaxation time. *Eur Phys J E* **34**, 30 (2011).
34. T. Yang, T. O. Tasci, K. B. Neeves, N. Wu, D. W. M. Marr, Magnetic microlassos for reversible cargo capture, transport, and release. *Langmuir* **33**, 5932-5937 (2017).
35. J. M. Dempster, P. Vazquez-Montejo, M. O. de la Cruz, Contractile actuation and dynamical gel assembly of paramagnetic filaments in fast precessing fields. *Phys Rev E* **95**, 052606 (2017).
36. P. Vazquez-Montejo, J. M. Dempster, M. O. de la Cruz, Paramagnetic filaments in a fast precessing field: Planar versus helical conformations. *Phy Rev Mater* **1**, 064402 (2017).
37. J. Gray, G. J. Hancock, The Propulsion of Sea-Urchin Spermatozoa. *J Exp Biol* **32**, 802-814 (1955).
38. E. M. Purcell, The efficiency of propulsion by a rotating flagellum. *P Natl Acad Sci USA* **94**, 11307-11311 (1997).
39. J. J. Abbott *et al.*, How Should Microrobots Swim? *Int J Robot Res* **28**, 1434-1447 (2009).
40. J. Lighthill, Flagellar hydrodynamics. *SIAM review* **18**, 161-230 (1976).
41. L. Turner, W. S. Ryu, H. C. Berg, Real-time imaging of fluorescent flagellar filaments. *J Bacteriol* **182**, 2793-2801 (2000).

42.   A. Vazquez-Quesada, T. Franke, M. Ellero, Theory and simulation of the dynamics, deformation, and breakup of a chain of superparamagnetic beads under a rotating magnetic field. *Phys Fluids* **29**, 032006 (2017).

43.   S. Lim, A. Ferent, X. S. Wang, C. S. Peskin, Dynamics of a Closed Rod with Twist and Bend in Fluid. *Siam J Sci Comput* **31**, 273-302 (2008).

44.   S. D. Olson, S. Lim, R. Cortez, Modeling the dynamics of an elastic rod with intrinsic curvature and twist using a regularized Stokes formulation. *J Comput Phys* **238**, 169-187 (2013).

45.   B. Sprinkle, E. B. van der Wee, Y. Luo, M. Driscoll, A. Donev, Active dynamics in dense suspensions of microrollers. *arXiv preprint arXiv:2005.06002* (2020).

46.   J. F. Brady, R. J. Phillips, J. C. Lester, G. Bossis, Dynamic Simulation of Hydrodynamically Interacting Suspensions. *J Fluid Mech* **195**, 257-280 (1988).

47.   J. W. Swan, J. F. Brady, Simulation of hydrodynamically interacting particles near a no-slip boundary. *Phys Fluids* **19**, 113306 (2007).

48.   F. B. Usabiaga, B. Delmotte, A. Donev, Brownian dynamics of confined suspensions of active microrollers. *J Chem Phys* **146**, 134104 (2017).

49.   M. Roper *et al.*, On the dynamics of magnetically driven elastic filaments. *J Fluid Mech* **554**, 167-190 (2006).

50.   E. E. Keaveny, M. R. Maxey, Spiral swimming of an artificial micro-swimmer. *J Fluid Mech* **598**, 293-319 (2008).

51.   M. Roper *et al.*, Do magnetic micro-swimmers move like eukaryotic cells? *Proc. R. Soc. A* **464**, 877-904 (2008).
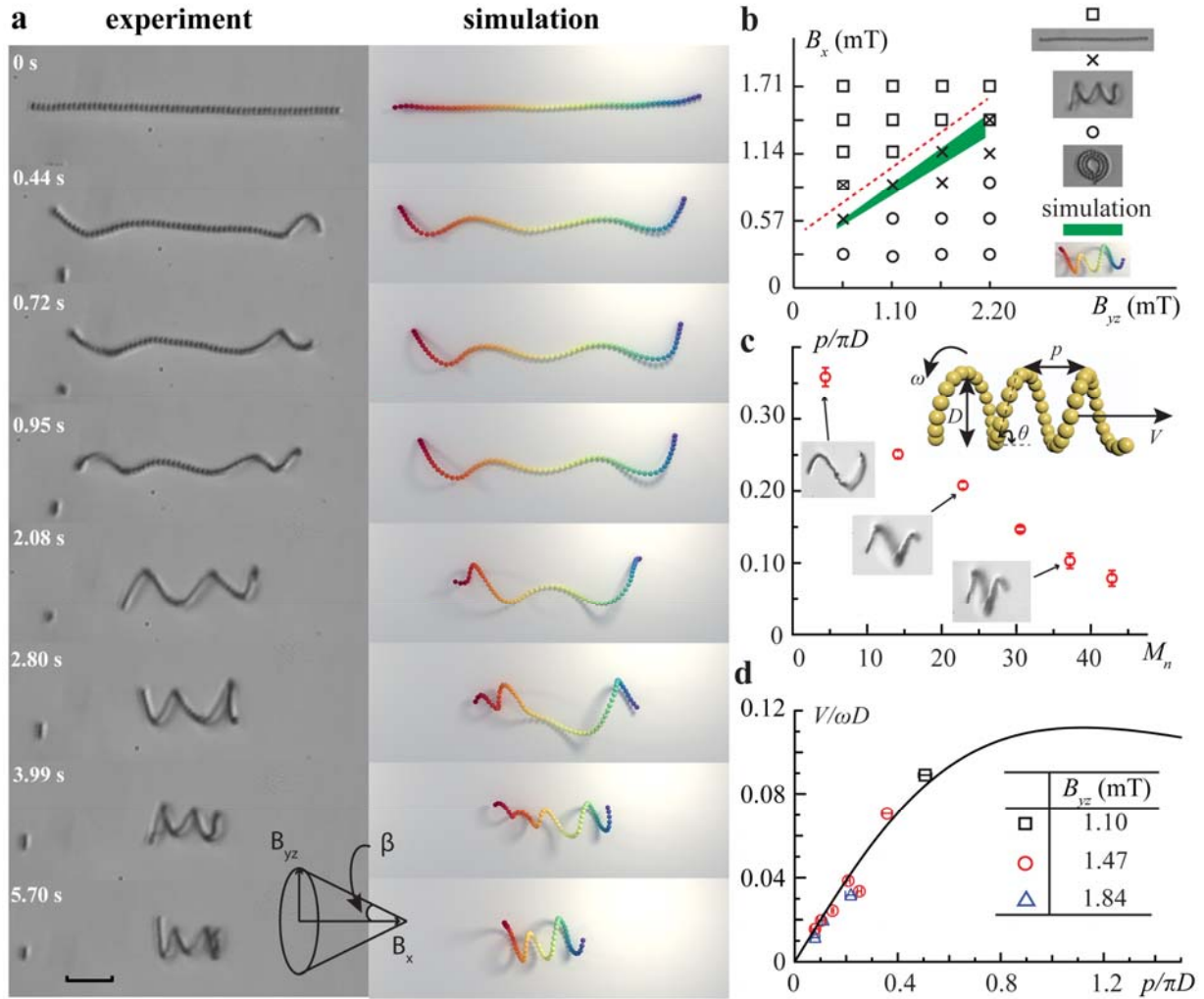
Fig. 1 Folding of magnetic chains under precessing magnetic fields. **a,** Snapshots showing the dynamics of chain folding in experiments (left) and simulations (right). Scale bar: 10 μm. **b,** The phase diagram of chain morphologies with varying field strengths in B_{yz} and B_x. The regime highlighted in green corresponds to the helix morphology predicted by numerical simulation. The red dash line corresponds to the magic cone angle $\beta = 54.7°$. **c,** The helical geometry ($p/\pi D$) with magnetoelastic constant M_n. The inset shows all relevant geometric parameters. The snapshots show the helix geometry at corresponding points. **d,** The propulsion efficiency ($V/\omega D$) of the helix as a function of its geometry for several strengths of the magnetic field (see inset) keeping the ratio B_x/B_{yz} fixed. The solid line comes from equation (5) with measured helix parameters p and D.
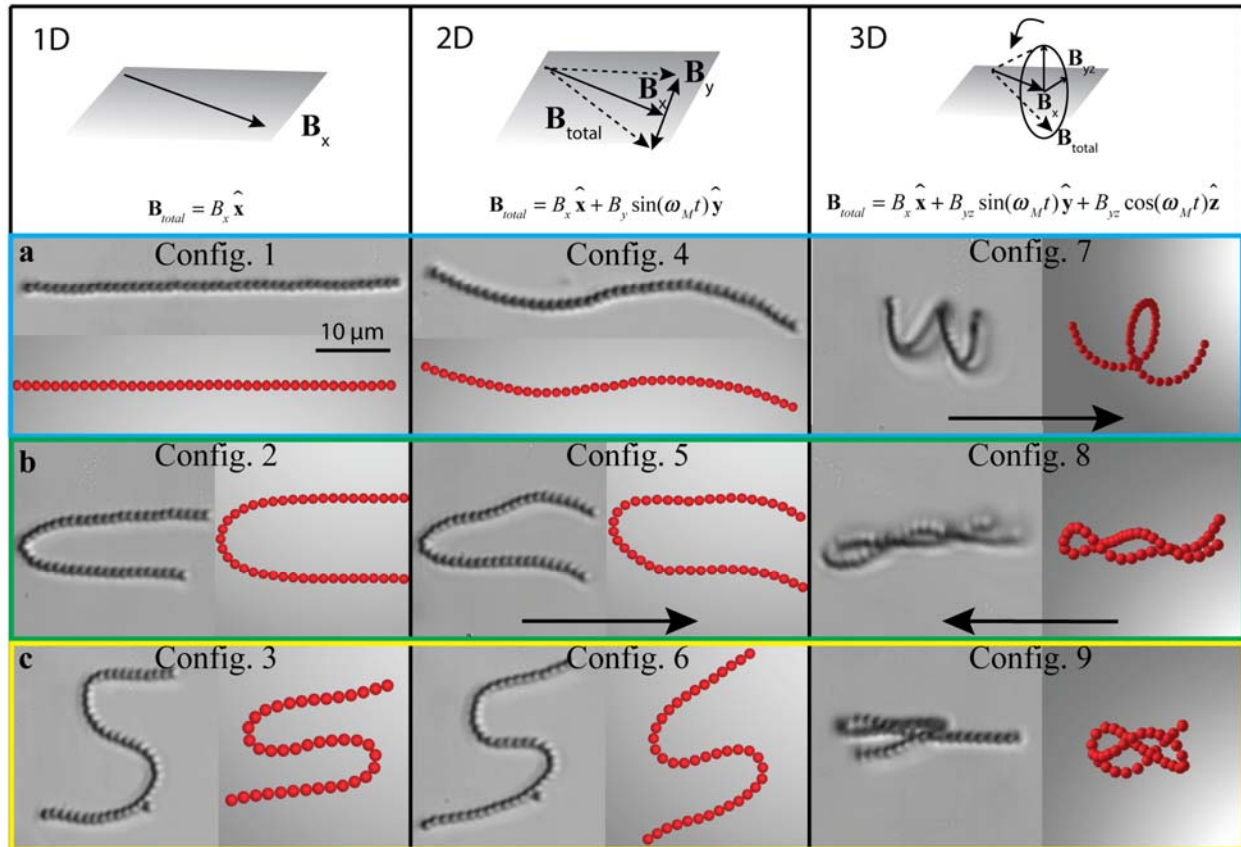
Fig. 2 Sequential folding and motion of a homogeneous chain under different magnetic field conditions in experiments (top or left half) and simulations (bottom or right half). **a,** Under a DC magnetic field, the chain can adopt line, U, and S shapes depending on initial conditions. **b,** By further applying an in-plane (*x-y*) undulatory magnetic field, they fold into oscillating arc, "U" and "S" shapes, respectively. **c,** The 3D precessing magnetic field makes the oscillating arc-, U-, and S-shaped chains to fold into helical, plectoneme, and coiled structures. The arrows indicate the net propulsion direction. The scale bar (10 μm) applies to all images.

2
3

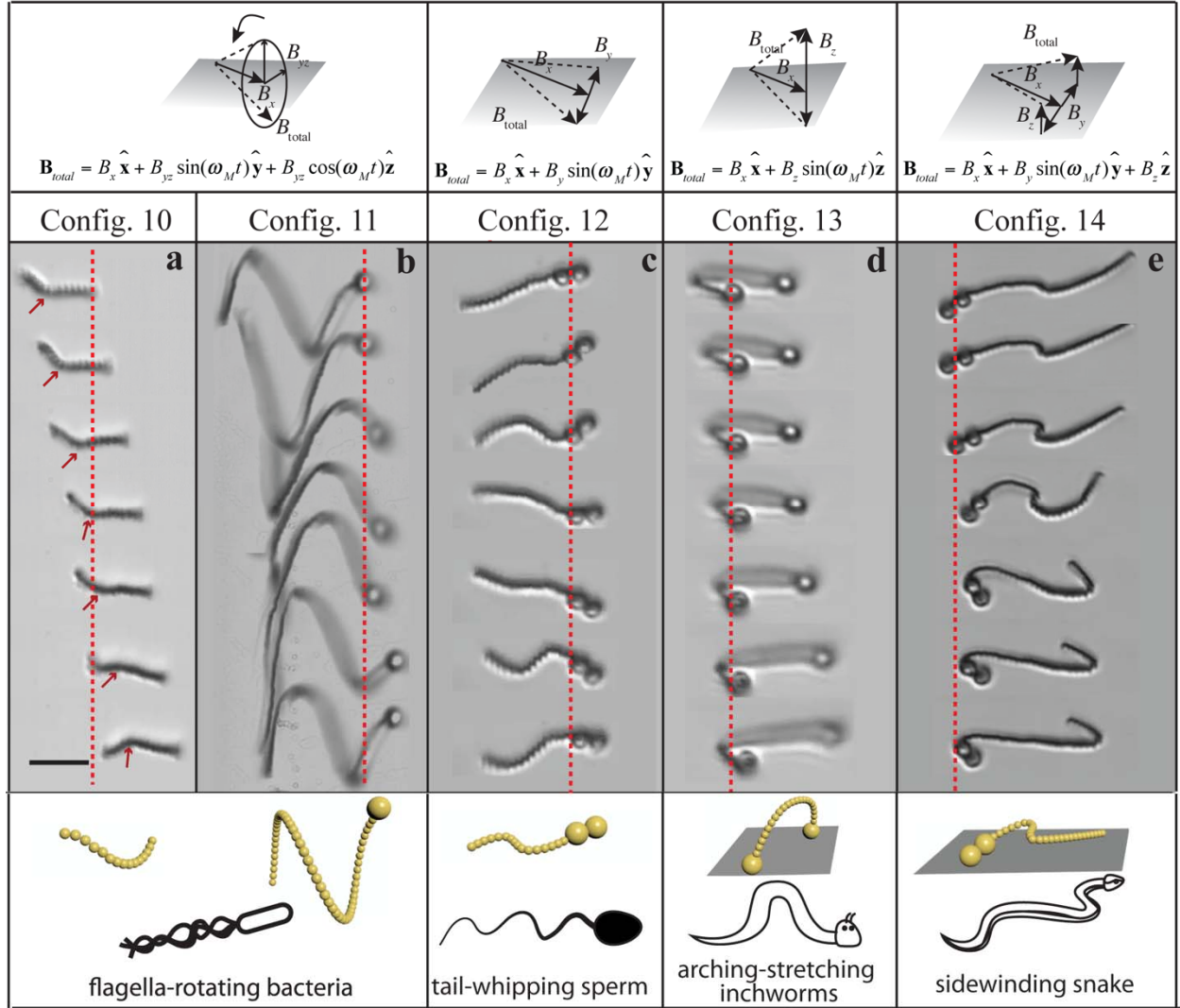| Config. 10	Config. 11	Config. 12	Config. 13	Config. 14
$\mathbf{B}_{total} = B_x\hat{\mathbf{x}} + B_{yz}\sin(\omega_M t)\hat{\mathbf{y}} + B_{yz}\cos(\omega_M t)\hat{\mathbf{z}}$		$\mathbf{B}_{total} = B_x\hat{\mathbf{x}} + B_y\sin(\omega_M t)\hat{\mathbf{y}}$	$\mathbf{B}_{total} = B_x\hat{\mathbf{x}} + B_z\sin(\omega_M t)\hat{\mathbf{z}}$	$\mathbf{B}_{total} = B_x\hat{\mathbf{x}} + B_y\sin(\omega_M t)\hat{\mathbf{y}} + B_z\hat{\mathbf{z}}$

flagella-rotating bacteria | tail-whipping sperm | arching-stretching inchworms | sidewinding snake

Fig. 3 Multimodal motion of heterogeneous chains that mimic natural swimmers and propellers. Snapshots in equal time intervals of 0.44s are shown top to bottom, with the red dashed line denoting a fixed reference position in the *x* direction. **a,** Rotation of a single block chain (14-mer) with a malformed point defect (red arrow, between the 5th and 6th particle) under a 3D precessing field. **b,** Helical motion of a diblock chain (54-mer tail with one 2.7 µm particle head) with a long and flexible tail under the same precessing field. Config. 10 and 11 mimic rotating bacteria flagella. **c,** In-plane undulatory motion of a diblock chain (13-mer tail with a 2 x 2.7 µm particle dimer head) under an *x-y* undulatory field, mimicking tail-whipping sperm. **d,** Inchworm motion of a triblock chain (21-mer chain with a 2.7 µm particle head and a 2.7 µm particle tail) under an *x-z* undulatory field, mimicking arching and stretching inchworms, and **e,** Sidewinding of a diblock chain (29-mer tail with a 2 x 2.7 µm particle dimer head) under a 3D undulatory magnetic field, mimicking sidewinding snakes. The scale bar (10 µm) applies to all images.
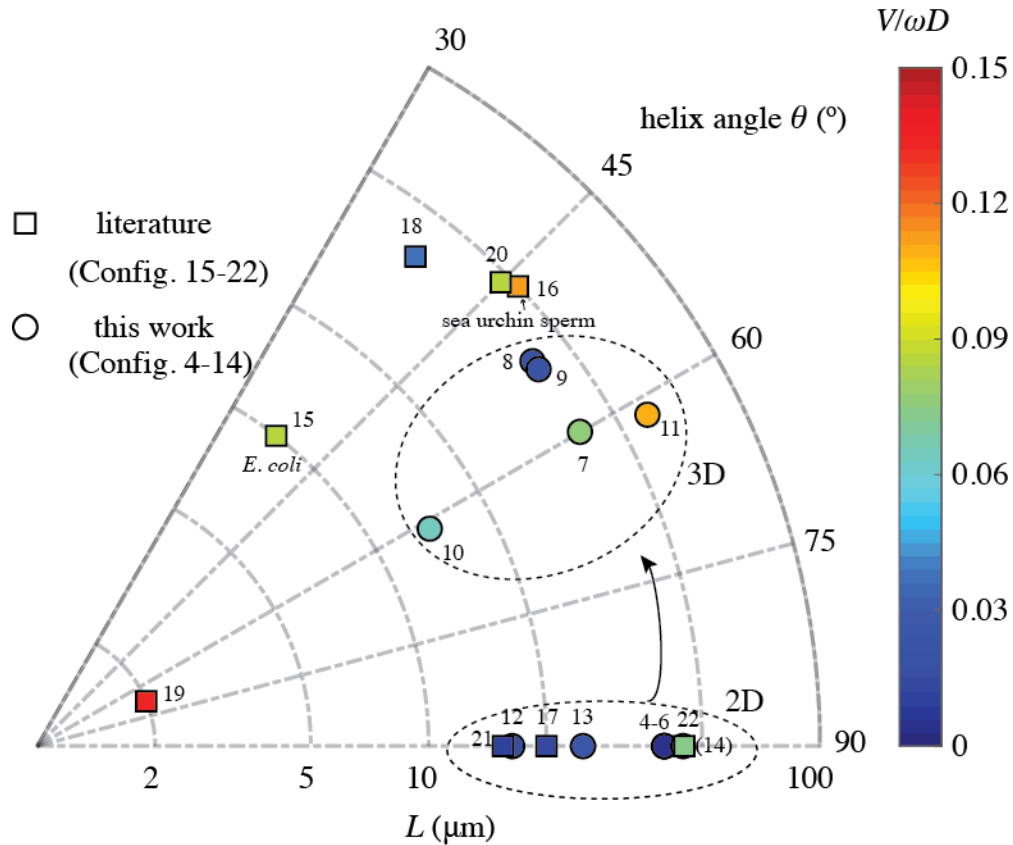
Fig. 4 Comparison of Config. 4-14 with microswimmers in the literature. The radius axis of the polar plot is the length scale, angle axis the helical angle θ in Fig. 1C inset. For 2D swimmers, $\theta = 90°$. The propulsion efficiency $V/\omega D$ is marked with different color in the colormap. For helical swimmers, D is the helix diameter. For 2D swimmers, D is twice the actuation amplitude. Config. 15 is the result from Turner, Ryu &Berg 2000 (41), 16 from Gray & Hancock 1955 (37), 17 from Dreyfus et al. 2005 (6), 18 from Zhang et al. 2009 (8), 19 from Ghosh et al. 2009 (7), 20 from Tottori et al. 2012 (9), 21 from Jang et al. 2015 (12), and 22 from Yang et al. 2017 (34).
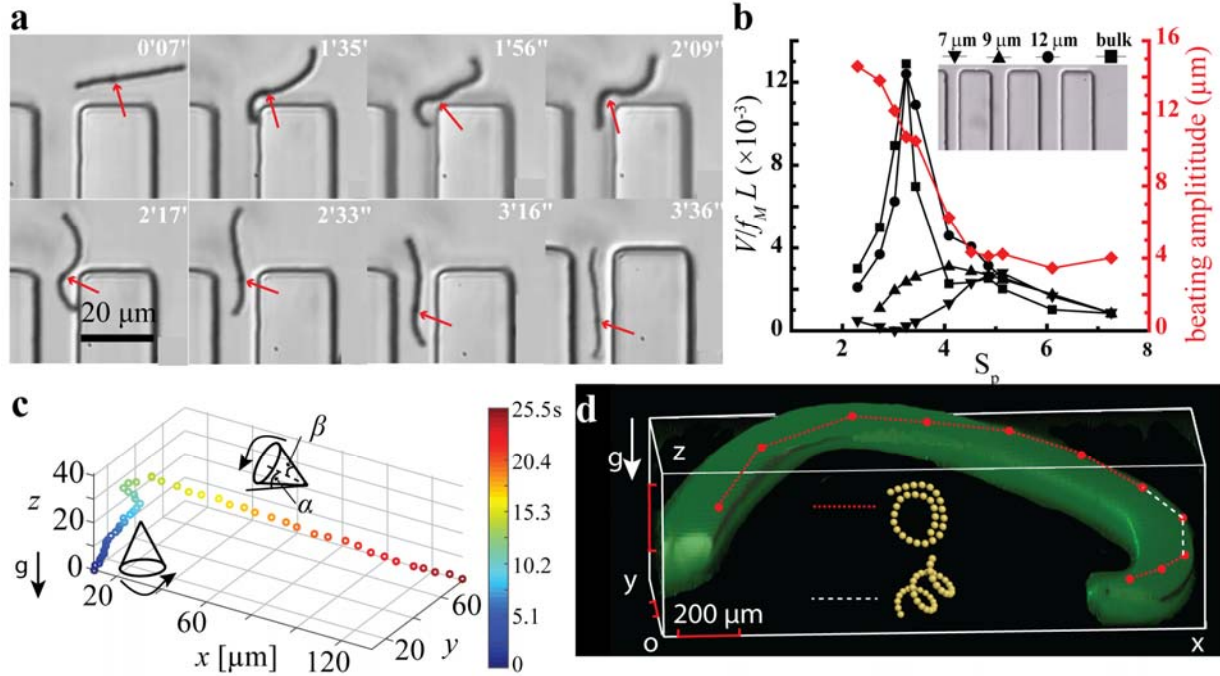
Fig. 5 Navigation of microchains into complicated environments including narrow channels and 3D curved channels. **a,** Typical dynamics of a defected linear chain (length ~ 21 μm) passing through a narrow channel (width 9 μm) under an in-plane undulatory magnetic field $B_x \hat{x} + B_y \sin(\omega_M t)\hat{y}$. The propulsion direction was controlled by the ratio of B_x and B_y. The red arrow indicates the point defect. **b,** The dependence of chain propulsion efficiency on the Sperm number $S_p = \left(\frac{2\pi f_M \zeta_\perp L^4}{k_{bend}}\right)^{\frac{1}{4}}$, in channels with different widths. The chain beating amplitudes were measured in bulk. **c,** Directed propulsion of a helical chain in bulk fluid by tuning the cone orientation α, including swimming against gravity (blue/green dots). We plot the 3D position of the center-of-mass of the chain as a function of time (indicated by the color scale). **d,** Multimodal chain propulsion within a 3D curved channel (1.78 x 0.80 x 0.55 mm, 3D reconstruction from confocal microscopy images and labelled by green fluorescent dyes) under tilted precessing magnetic fields. The red dots indicate chain positions every two minutes. The segments connecting the red dots indicate sections of the trajectory where the chain is a helix (white) or a lasso (red), as controlled via the magnetic field.

Reconfigurable microbots folded from simple colloidal chains

Tao Yang[1], Brennan Sprinkle[2], Yang Guo[1], Jun Qian[3], Daoben Hua[3], Aleksandar Donev[2], David W.M. Marr[1]*, and Ning Wu[1]*

[1]Department of Chemical and Biological Engineering, Colorado School of Mines, Golden, Colorado, USA 80401

[2]Courant Institute of Mathematical Sciences, New York University, New York, New York, USA 10012

[3]State Key Laboratory of Radiation Medicine and Protection, School for Radiological and Interdisciplinary Sciences (RAD–X), Soochow University, Suzhou, China 215123

*E-mail:ningwu@mines.edu

*E-mail:dmarr@mines.edu

Supporting information

1.   **Experimental Section**

1.1   **Materials**

Dynabeads™ Myone™ carboxylic acid ($2a$ =1.05 μm, surface group ~0.6 mmol/g) and M-270 carboxylic acid ($2a$ = 2.8 μm) were purchased from Thermo Fisher Scientific. N-(3-Dimethylaminopropyl)-N′-ethylcarbodiimide hydrochloride (EDC), n-hydroxysuccinimide (NHS, 98%), cysteamine (~95%), dimethyl sulfoxide (DMSO, $\geq 99.9\%$), and 1,8-Diazabicycloundec-7-ene (DBU) were purchased from Sigma-Aldrich. 4-arm PEG-maleimide (M_w=40k) obtained from JenKem Technology (Beijing, China). Measure-IT™ thiol assay kit (Cat. No. M30550) was purchased from Invitrogen. All chemicals were used as received.

1.2   **Thiolation of Dynabeads**

Particle surface modification and chain fabrication are illustrated in Fig. S1A. In this, carboxylic acid surface groups were first activated via carbodiimide chemistry with EDC/NHS (Step 1). The intermediate (NHS ester) was then reacted with cysteamine overnight to form a stable amide bond (Step 2). As a result, some of the carboxylic acid groups were converted into thiols. 100 µL Dynabeads™ Myone™ carboxylic acid (10 mg/mL, carboxylic acid ~ 0.6 µmol) (or 130 µL M-270 carboxylic acid) were first washed and re-dispersed into 10 mL DI water. 3.8 mg EDC (~0.02 mmol) and 2.3 mg (~0.02 mmol) NHS were then added into the particle suspension and incubated at room temperature for 2 hr. Afterwards, 0.046 mg (0.6 µmol) or 0.46 mg (6 µmol) cysteamine, representing approximately 1x or 10x of the number of available carboxylic acid functional groups on Dynabeads in 100 µL solution, was added into the mixture and incubated overnight. The thiolated magnetic particles were then centrifuged and washed 3x with DI water followed by a 2x wash with DMSO after the reaction was completed. Finally, the surface-modified particles were suspended in 4 mL DMSO.

1.3   Fabrication of flexible magnetic chains

Because of its fast kinetics and high efficiency, a thiol-maleimide Michael addition reaction was utilized to build linkages between particles as in our previous work (1). To fabricate magnetic chains, we mixed 95 µL thiolated Dynabead Myone™ (suspended in DMSO) with 95 µL 10 mg/mL 4-arm PEG-maleimide solution (dissolved in DMSO and filtered) and 10 µL 3 µL/mL DBU (as catalyst) solution (dissolved in DMSO and filtered) in a square cuvette with screw cap. As illustrated in Fig. S1B, we placed the cuvettes inside a magnetic coil and immersed both cuvettes and coils inside a large oil bath (maintained at 75 °C) to not only provide a more stable reaction temperature but also to cool coils under high current. We then applied a one-dimensional DC magnetic field (~60 mT) along the vertical direction. The magnetic fields

were produced by air-cored copper coils of 2.83" inner diameter, 1.18" length, 12 mH inductance, and 18 AWG wire gauge. The current passed through the coils was generated with a DC power supply. With the application of the magnetic field, particles assembled into linear chains aligned parallel with the field. For homogeneous chains, after 0.5 hr, the magnetic field was turned off. To fabricate heterogeneous diblock chains, thiolated Dynabead Myone™ were first assembled for 15 mins, 5 µL thiolated Dynabead M-270 was then added and the field was left on for another 15 mins. After fabrication, cuvettes and coils were removed from the oil bath and left to cool gradually to room temperature. The fabricated chains were then washed with DMSO 3x to remove excess PEG and DBU.

1.4 Fabrication of straight and curved PMDS channels

Straight channels were fabricated using standard soft lithography techniques (2). KMPR1010 was used as photoresist and a patterned photomask with 2 µm resolution was purchased from Front Range Photomask, LLC. The curved 3D channels were fabricated using a scaffold-removal method reported previously (3). In this and briefly, a thin, curvy acrylonitrile butadiene styrene (ABS) thread was immersed in a PDMS precuring and degassed solution (5:1 polymer:curing agent mass ratio) and cured for 4 hrs at 80 °C. The PDMS device was then left in acetone overnight to remove the ABS scaffold after which 3D channels were cleaned with acetone followed by air drying.

1.5 Characterization

Thiol functional groups on the surface-modified Dynabeads were quantified using a microplate reader (Synergy H1 Hybrid Multi-Mode Microplate Reader, BioTek, Winooski, VT) with the Measure-IT™ thiol assay kit following the established procedures. Chain length and morphology were characterized by scanning electron microscopy (SEM, JEOL JSM-7000F) and

transmission electron microscopy (TEM, FEI TALOS F200X CTEM/STEM). Bright-field

optical images were obtained with a color camera (Retiga 2000R) connected to an inverted

microscope (Olympus IX71). Videos were taken using a CCD camera (SV643M). We used a

confocal microscope (10X, NA = 1.2, Olympus FV10i) to identify the 3D structure of the curved

channel where 0.01% Nile red dissolved in heavy mineral oil was injected into the channel to

provide good fluorescence contrast. Heavy mineral oil was selected to prevent solvent from

evaporating during the confocal scanning. The entire channel section was made of 2 × 2 local

scanning (1300 μm × 1300 μm for each image) with 30 z-stack images (10 μm interval) at each

position. After the measurement was completed, images were stitched together with ImageJ.

1.6   Chain actuation under magnetic fields

Three-dimensional time varying magnetic fields were generated and controlled in the

same manner as our previous work (4-6). Briefly, the current signals from an output card (National

Instruments, NI-9263) were amplified by amplifiers (BOP-40-5m) and then passed through air-cored

copper solenoid coils (50 mm inner diameter, 51 mm length, and 400 turns with current capacity of 3.5

A). Signals were programmed using Matlab (Mathworks, Inc.). In-time signal monitoring was performed

via data card (National Instruments, NI-USB-6009) and gaussmeter (VGM Gaussmeter, Alphalab, Inc).

Chain propulsion was captured at a frame rate of 50 fps with a CCD camera (Epix, Inc., SV643M)

mounted on a microscope (Carl Zeiss, Axioplan 2). Instantaneous velocities were then obtained by

calculating displacement over a time interval of $\Delta t = 0.04$s. Chain rotational frequency was determined

via Fourier transform of the measured instantaneous velocities. The power amplifier that drives the

copper coils operates in the range 20-200 Hz, limiting the choice of the precessing field

frequency. Janssen, *et al.* (7) have shown that single magnetic particles rotate synchronically

with the external field at low frequencies. With increasing frequency, the induced diploe cannot

follow with the field and particle rotation speed drops off to zero. This critical transition

4

frequency, from synchronized to asynchronized rotation, varies between 1-10 Hz depending on field strength. At much higher frequencies (e.g., > 1000 Hz), the particle may rotate again as the imaginary part of particle susceptibility arises due to Neel relaxation (7). We expect our chain rotation will follow the similar trend as the chains consist of the same type of magnetic particles in those studies.

1.7   Determination of chain flexibility

Chain flexibility was measured using methods reported previously (1, 8). Briefly, a colloidal chain was aligned initially by DC field along the x-axis. A sudden orthogonal switch of the magnetic field direction from the x to y axis causes the straight chain to bend into a U-shaped arc. With measurement of the steady-state separation Δ between the two parallel legs for different field strengths, the chain bending modulus $\kappa_{bend} = EI$ (E is the Young's modulus and $I = \pi a^4 / 4$ is the moment of inertia) can be calculated following (1, 8)

$$\frac{2\pi}{\Delta} = \chi Ba \sqrt{\frac{\pi}{6k_{bend}\mu_0}} \tag{S1}$$

where χ is the magnetic susceptibility of individual particles, B is the magnetic flux density, and μ_0 is the permeability of free space.

2.   Characterization of particle surface modification and magnetic chain fabrication

Particle surface modification was verified by Fourier-transform infrared spectroscopy (FTIR) shown in Fig. S1C with the appearance of peaks corresponding to NHS ester (~1730 cm^{-1}) and amide I (~1660 cm^{-1}). Approximately, 3.8% and 24.8% carboxyl functional groups were converted into thiols for 0.046 mg (1x) and 0.46 mg (10x) cysteamine, respectively. Further evidence of thiolation was provided by a change of zeta potentials after surface modification and energy-dispersive X-ray (EDX) analysis of the sulfur element as shown in Table S1 and Fig.

S2D. With higher thiol surface coverage, we obtain greater average chain length and higher chain rigidity. With a goal of longer and flexible chains, we fixed fabrication conditions of strong magnetic field (60 mT) and low surface thiol coverage (1x or 0.046 mg). Fabricated chain morphologies are shown in Fig. S2A-C.

3.   Numerical simulation

The colloidal chain was modeled as linked spherical beads of radius a using the minimally resolved Stokesian dynamics method (9) with thermal fluctuations. The method uses the Rotne–Prager–Blake (10) tensor to compute the translational and rotational hydrodynamic mobility between particles of radius a suspended above a bottom wall. We included near-field lubrication corrections to the hydrodynamics following Brady *et al.* (11, 12) for both neighboring pairs of particles along the magnetic chain and between individual particles and the bottom wall. To evolve the fluctuating dynamics of the chains, the method developed in (9) uses a trapezoidal temporal integration scheme (similar to the scheme developed in (13)), which accounts for lubrication corrections in the Brownian dynamics. We found that, while including Brownian motion is not essential to simulate the qualitative dynamics of the particle chains including the formation of rotating helices, it did ensure that rotating helices formed in realistic time scales that were consistent with experiments.

While the chains that we simulate in this work are composed of a modest number of discrete beads, past work (14, 15) has used continuous models of elastic fibers parameterized by their arclength s to derive formulas for the internal forces and torques on chains of beads. A continuous fiber of length L is described by the curve $\boldsymbol{x}(s)$, $s \in [0, L]$, where for an inextensible fiber $||\partial_s \boldsymbol{x}||_2 = 1$. The rods orientation along its length is described by a continuously varying unit triad $\{\boldsymbol{D}_1(s), \boldsymbol{D}_2(s), \boldsymbol{D}_3(s)\}$, where $\boldsymbol{D}_3(s)$ is constrained to align with the unit tangent vector

along the chain $\partial_s x$. The fiber can be discretized with beads placed at locations $x_i \approx x(s_i = iL/N)$, $i = 0, \dots, N$, where each bead has an associated unit triad $\{D_1^i, D_2^i, D_3^i\}$ such that $D_3^i = \frac{(x_{i+1}-x_i)}{2a} = \hat{r}_{i+1,i} \approx \partial_s x(s_i)$. In our computational methods we used a unit quaternion to represent the orientation of each bead (16, 17).

Following Lim *et al.* (14), Olson *et al.*(15) described the internal force and torque densities f^{internal} and t^{internal} on the chain of beads by discretizing the continuous formula for fibers,

$$f^{\text{internal}} = -\frac{\partial F^{\text{constrain}}}{\partial s} \tag{S2}$$

$$t^{\text{internal}} = -\frac{\partial M^{\text{internal}}}{\partial s} - \frac{\partial X}{\partial s} \times F^{\text{constrain}} \tag{S3}$$

where $F^{\text{constrain}}$ is a penalty force that ensures that for each particle along the chain $D_3(s)$ is aligned with the tangent vector $\hat{r}_{i+1,i}$ and that the chain is approximately inextensible (14). For a discrete chain these force densities directly translate into forces on each bead $F_i \approx 2af^{\text{internal}}(s_i)$ and $T_i \approx 2at^{\text{internal}}(s_i)$. In this formulation there are a total of 6 coefficients in the constitutive laws, two bending moduli $a_1 = a_2$ and one twisting modulus $a_3 = \kappa_{\text{twist}}$ defining M^{internal}, and three penalty moduli defining $F^{\text{constrain}}$ -- two shear moduli $b_1 = b_2$ and one extension modulus b_3 (14).

Explicit formulas for the constraint forces $F^{\text{constrain}}$ on the discrete beads in terms of the triad vectors are given by equations (4a–5b) in Ref. (15); we set the extension modulus and the shear moduli $b_3 = b_1 = b_2 = 1$ pN. To ensure nearly strict inextensibility in the chain we add an additional penalty force coming from a harmonic spring between neighboring beads of stiffness $\kappa^{\text{spring}} \approx 10^{-5} N/m$ with a rest length $l_{\text{rest}} \approx 2a$.

Following equation (49) in Schoeller *et al.*(17), we used a convenient form in terms of unit quaternions to compute the internal moments $\boldsymbol{M}^{\text{internal}}$, assuming an unstressed or intrinsically straight chain. Both Schoeller *et al.* (17) and Olson *et al.*(15) gave similar discretization of the arclength derivatives required in equation (S3); we used equations (30-31) in Olson *et al.*(15) as this work uses an explicit penalty approach. The chain dynamics are sensitive to the value of the twisting modulus $a_3 = \kappa_{\text{twist}}$ representing the tendency of the chain to resist torques applied in the direction tangent to the chain. This value cannot be measured experimentally, and in this work we used $\kappa_{\text{twist}} = 2.6 \times 10^{-25}$ J·m. We set the bending moduli $a_1 = a_2 = 0$ since we account for bending elasticity separately; similar results are obtained by setting $a_1 = a_2 = \kappa_{\text{bend}}$ and not separately including the elastic force density in equation (S4).

Specifically, we take the elastic force density due to bending to be given by

$$\boldsymbol{F}^{\text{bend}} = -\kappa_{\text{bend}}(s)\frac{\partial^4 \boldsymbol{x}}{\partial s^4},$$

$$\frac{\partial^3 \boldsymbol{x}}{\partial s^3}\Big|_{s=0} = \frac{\partial^3 \boldsymbol{x}}{\partial s^3}\Big|_{s=L} = \frac{\partial^2 \boldsymbol{x}}{\partial s^2}\Big|_{s=0} = \frac{\partial^2 \boldsymbol{x}}{\partial s^2}\Big|_{s=L} = 0.$$

(S4)

Explicit discrete formulas for the bending forces on each bead are given in equation (5) in Ref. (18). In the majority of the simulations reported here, we set $\kappa_{bend} = \kappa_{bend}^{const} = 2.0 \times 10^{-24}$ J·m, except that for Fig. 1A and movie S1 we took the bending modulus to be variable along the length of the chain such that

$$\kappa_{bend}(s) = \kappa_{bend}^{const}\frac{3+2(s/L)}{5}.$$

(S5)

This variable form of $\kappa_{bend}(s)$ was chosen *ad hoc* to give the chain some flexural heterogeneity and hence break the bending symmetry between the two ends of the chain. The bending forces and modulus are validated against experiments in Fig. S3.

4. Estimation of the number of PEG linkers between neighboring chain particles

For a single PEG chain and in the low stretching force limit, the Hook's spring constant $k_0 = 3k_BT/R_g^2$, where k_BT is the thermal energy and R_g is the radius of gyration (19). For 4-arm 40k PEG with a "cross" shape, its effective molecular weight along one direction is 20k (20) leading to $k_0 = 0.58$ mN/m. If we instead assume that multiple polymer chains connect neighboring particles and form a rod of length R_g with effective contact radius y (Fig. S5), then Hook's spring constant between neighboring particles linked by multiple polymer chains k_{tot} can be related to the effective Young's modulus of the polymer tether E_{eff} via $k_{tot} = \frac{E_{eff}\pi y^2}{R_g} = \frac{4\kappa_{bend}}{y^2 R_g}$, where κ_{bend} is the colloidal chain bending modulus (7). Based on our chain bending experiments, $\kappa_{bend} \sim 10^{-24} - 10^{-26}$ J·m and $y \sim 100$ nm determined from our previous work (1) leading to $k_{tot} = 0.91 - 91\ m$N/m. Assuming that the PEG linkers are springs connected in parallel, we estimate the number of polymer linkers between neighboring particles ranges from $N = \frac{k_{tot}}{k_0} \sim 2$ to 160, depending on the linker concentration during chain synthesis.
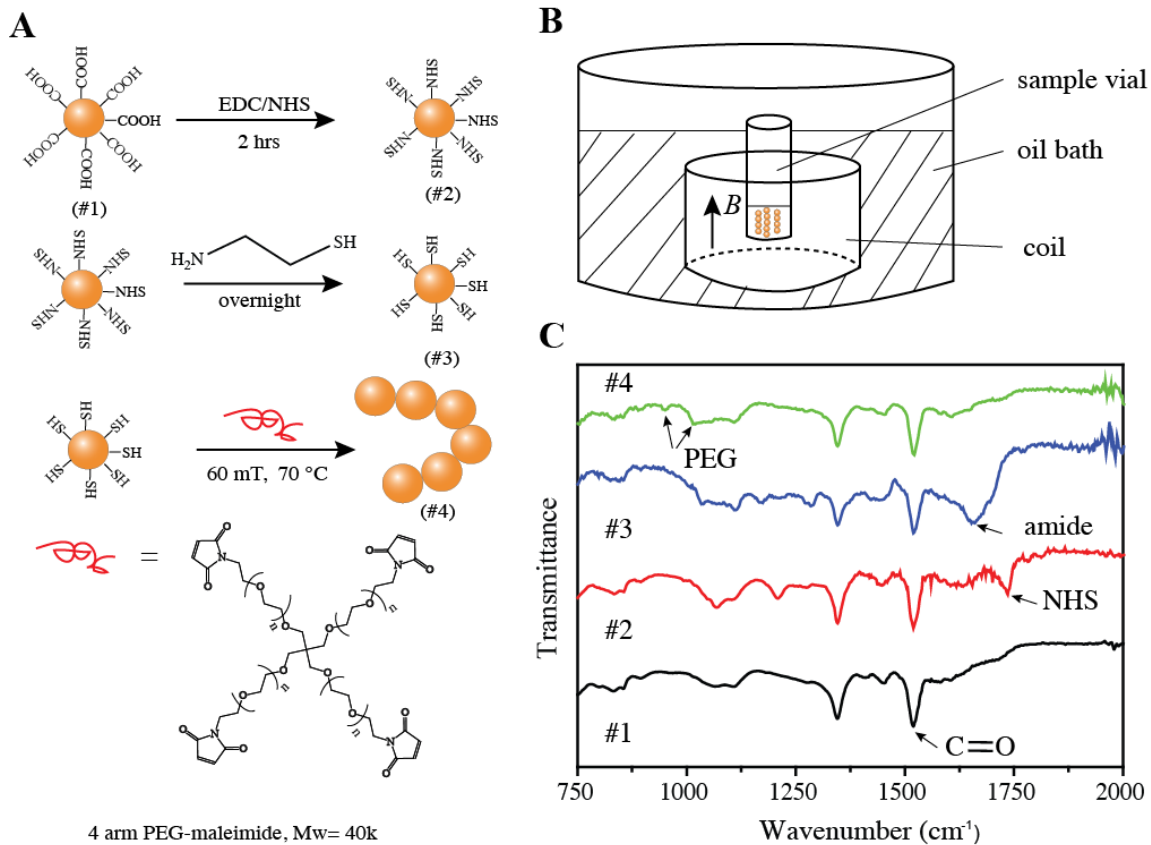
Figure S1 The surface modification of magnetic particles (Dynabead Myone™) and fabrication of chains. (A) Schematics showing particle surface modification and chain linking strategy. (B) Schematics of chain fabrication setup. (C) FTIR measurement of the surface-modified particles from each step in A.
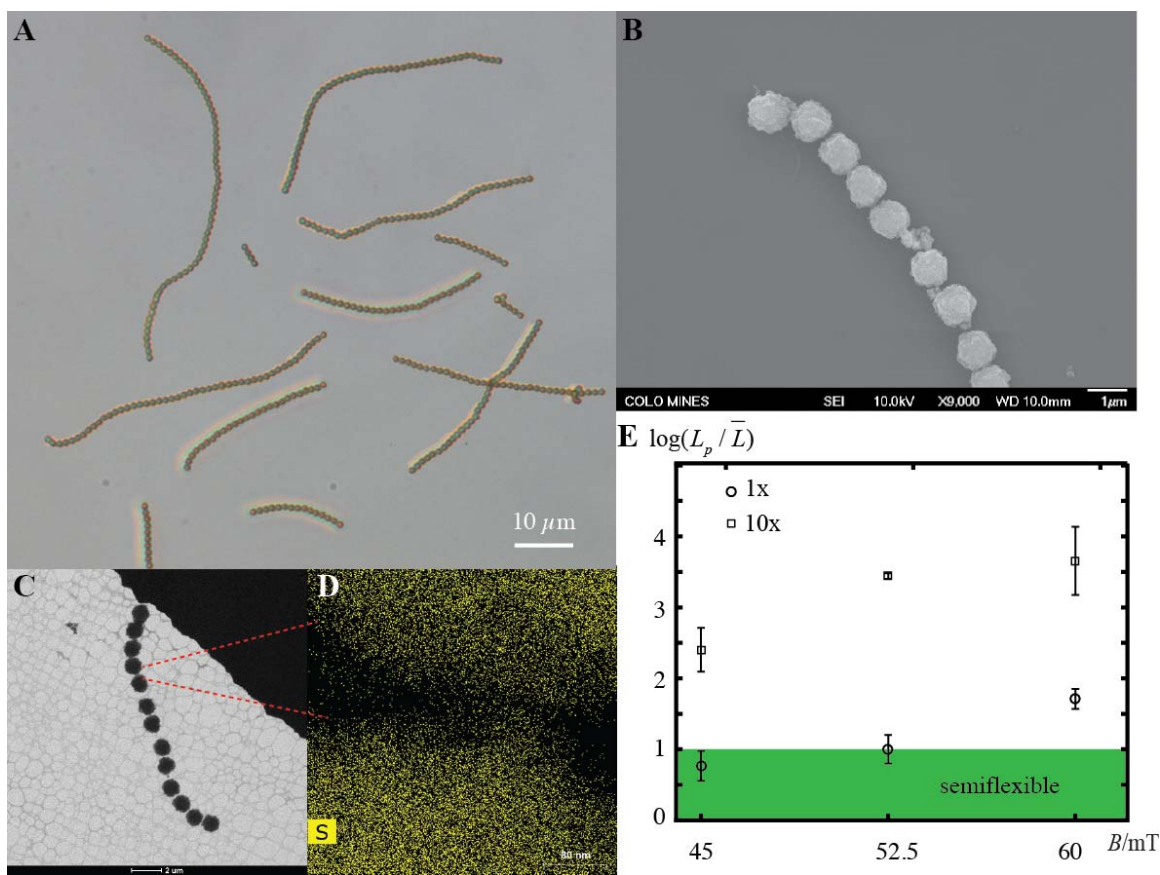
Figure S2 Characterization of fabricated magnetic chains. (A) Light microscopy, (B) SEM, and (C) TEM images of magnetic chains fabricated at 70 ℃, 60 mT for 30 min. (D) EDX (sulfur) mapping of two-neighboring particles inside a chain. (E) The ratio of magnetic chain persistent length ($L_p = EI/k_BT$) to average chain length $\bar{L}$ fabricated with different magnetic flux densities and particle surface thiol concentrations (see Table S1). The green area represents the semiflexible region with a ratio $\bar{L}/L_p$ from 1 to 10.
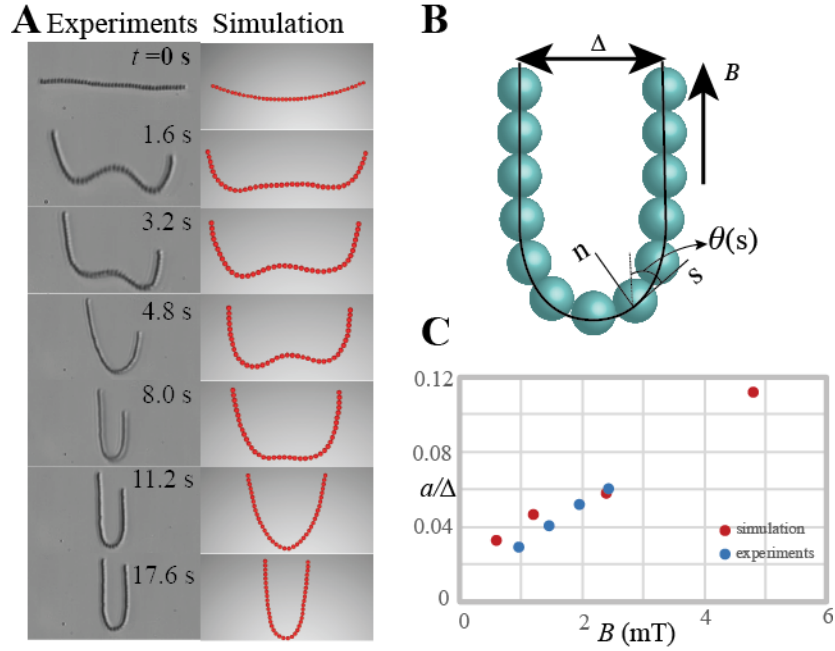
Figure S3 The bending of a colloidal chain into U-shape. (A) Comparison between simulation and experiments under identical magnetic field conditions. (B) Schematic of chain bending. (C) Dimensionless chain curvature a/Δ vs. magnetic flux density B.
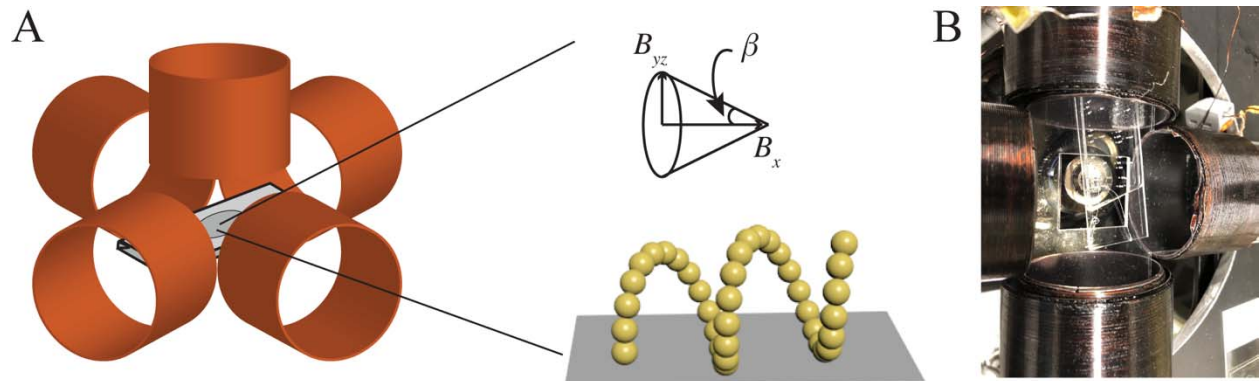

Figure S4 3D magnetic field setup. (A) Schematic. (B) Experimental setup with coil diameters of 5 cm and the 3D microfluidic channel.
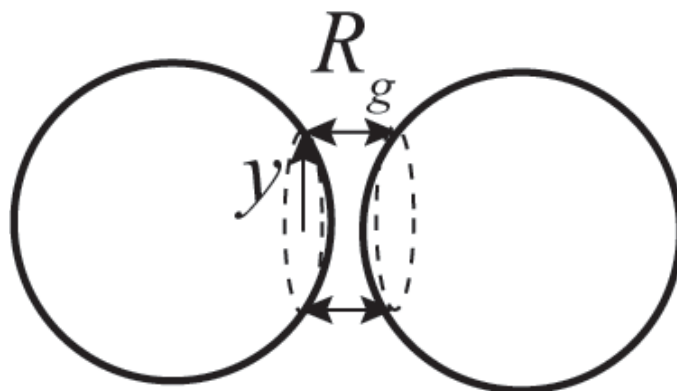
Figure S5 Schematic of polymer linkage between neighboring particles, which is considered as a rod of length R_g and radius of contact of y, where R_g is the polymer radius of gyration (8). The linker and particles are not drawn to scale.

Table S1 Characterization of particle modification from step 1-2 in Fig. S1A

	Zeta potential/mV	Thiol concentration/ ($\mu mol/g$)	Conversion rate[*]
Unmodified beads	-69.7±2.9	N.A.	N.A.
1x	-51.2±0.7	22.8	3.8%
10x	-36.4±2.1	149.0	24.8%

*Assuming particle surface group concentration of 300 µmol/g per the product manual.

Table S2 Simulation parameters used in Fig. 1A and Fig. 2.

Fig.	Config.	$\dfrac{\Delta k_{bend}}{k_{bend}}$	$F_{0,x}$[pN]	$f_{M,x}$ [Hz]	$F_{0,y}$[pN]	$f_{M,y}$ [Hz]	$F_{0,z}$[pN]	$f_{M,z}$ [Hz]
1A[2]	N.A.	40%	1.22	0[1]	2.3	50	2.3	50
2	4, 5, 6	0	0.462	0	0.42	0.5	0	0
2[2]	7	0	3.44	0	5.83	10	5.83	10
2[2]	8, 9	0	4.5	0	5.83	10	5.83	10

Note: $\kappa_{bend} = \kappa_{bend}^{const} = 2.0 \times 10^{-24}$ J·m for all simulations.

[1.] 0 Hz is application of a DC field.
[2.] Precessing fields: $F_{0,x} = F_0 * \cos\beta$, $F_{0,x} = F_0 * \sin\beta$.

4. List of supplementary movies

Movie S1 Folding a linear colloidal chain into a helix under a precessing magnetic field (experiment vs simulation) (Fig. 1A): $B_x\hat{\mathbf{x}} + B_{yz}\sin(\omega_M t)\hat{\mathbf{y}} + B_{yz}\cos(\omega_M t)\hat{\mathbf{z}}$, where $B_x = 1.75$ mT, $B_{yz} = 3.88$ mT, and $\omega_M = 314$ rad s^{-1}. The movie is displayed in real time. For the simulation, simulation parameters are listed in Table S2.

Movie S2 Propulsion of a helix, rolling of a lasso, and rolling of a rigid rod under a precessing magnetic field: $B_x\hat{\mathbf{x}} + B_{yz}\sin(\omega_M t)\hat{\mathbf{y}} + B_{yz}\cos(\omega_M t)\hat{\mathbf{z}}$. For the helix, $B_x = 2.0$ mT, $B_{yz} = 3.88$ mT, and $\omega_M = 314$ rad s^{-1}; for the lasso, $B_x = 1.33$ mT, $B_{yz} = 3.88$ mT, and $\omega_M = 314$ rad s^{-1}; for the rod, $B_x = 2.22$ mT, $B_{yz} = 2.77$ mT, and $\omega_M = 314$ rad s^{-1}. The movies are displayed in real time.

Movie S3 Experiment and simulation showing the bending of a straight chain into U shape under same magnetic field strength ($B_y = 2.22$ mT). The experimental movie is displayed in real time. The simulation movie is displayed with time stamps in second. See Fig. S3A for snapshots at the same point in time.

Movie S4 First part: experiment showing sequential folding of chains into U-shape and plectoneme; second part: simulation showing a chain folding into a plactonome and a coiled configuration. For the U-shape, an in-plane oscillating magnetic field: $B_x\hat{\mathbf{x}} + B_y\sin(\omega_M t)\hat{\mathbf{y}}$ was applied and $B_x = 1.16$ mT, $B_{yz} = 1.94$ mT, and $\omega_M = 3.14$ rad s^{-1}. The movie is accelerated 2x. For the plectoneme, a precessing magnetic field $B_x\hat{\mathbf{x}} + B_{yz}\sin(\omega_M t)\hat{\mathbf{y}} + B_{yz}\cos(\omega_M t)\hat{\mathbf{z}}$ was applied and $B_x = 0.97$ mT, $B_{yz} = 1.94$ mT, and $\omega_M = 314$ rad s^{-1}. The movie is displayed in real time. For the simulation, simulation parameters are listed in Table S2.

Movie S5 Helical motion of diblock chains under a precessing magnetic field (Fig. 3A and 3B): $B_x\hat{\mathbf{x}} + B_{yz}\sin(\omega_M t)\hat{\mathbf{y}} + B_{yz}\cos(\omega_M t)\hat{\mathbf{z}}$. For 3A, $B_x = 1.66$ mT, $B_{yz} = 3.33$ mT, and $\omega_M = 314$ rad s^{-1}; for 3B, $B_x = 1.44$ mT, $B_{yz} = 3.88$ mT, and $\omega_M = 314$ rad s^{-1}. All movies are displayed in real time.

Movie S6 Fig. 3C. Undulatory motion of a diblock chain under an in-plane oscillating magnetic field: $B_x\hat{\mathbf{x}} + B_y\sin(\omega_M t)\hat{\mathbf{y}}$, $B_x = 2.10$ mT, $B_y = 1.90$ mT, and $\omega_M = 25.12$ rad s^{-1}. The movie is accelerated 1.5x.

Movie S7 Arching and stretching inchworm motion of a triblock chain under a 3D oscillating magnetic field: $B_x\hat{\mathbf{x}} + B_z\sin(\omega_M t)\hat{\mathbf{z}}$, $B_x = 1.90$ mT, $B_z = 4.24$ mT, and $\omega_M = 12.56$ rad s^{-1}. The movie is displayed in real time.

Movie S8 Snake-like sidewinding motion of a diblock chain under a 3D oscillating magnetic field: $B_x\sin(\omega_M t)\hat{\mathbf{x}} + B_y\hat{\mathbf{y}} + B_z\hat{\mathbf{z}}$, $B_x = 3.40$ mT, $B_y = 0.82$ mT, $B_z = 1.77$ mT and $\omega_M = 12.56$ rad s^{-1}. The movie is accelerated 3x.

Movie S9 Navigation of a undulatory magnetic chain ($L \sim 21$ µm) into a narrow channel (width ~ 8.58 µm). The applied magnetic field conditions are: $B_x \hat{\mathbf{x}} + B_y \sin(\omega_M t)\hat{\mathbf{y}}$, $B_x = 0.97$ mT, $B_y = 0.97\text{-}1.94$ mT, and $\omega_M = 12.56$ rad s^{-1}, and B_y was varied to control the propulsion direction. The movie is accelerated 10x.

Movie S10 Fig. 5C. 3D propulsion of a single block in bulk under a titled precessing field. The movie is displaced in real time. In the 1$^{\text{st}}$ part, the cone is orientated towards z axis; for the 2$^{\text{nd}}$ part, the cone orientation $\alpha \sim 60°$. For both cases, , $B_{\text{DC}} = 2.22$ mT, $B_{\text{AC}} = 2.77$ mT, and $\omega_M = 314$ rad s^{-1}.

Movie S11 Fig. 5D. Navigation of a chain through 3D channels. The movie is accelerated 10x.

References

1.	T. Yang, D. W. M. Marr, N. Wu, Superparamagnetic colloidal chains prepared via Michael-addition. *Colloids Surf. A Physicochem. Eng. Asp.* **540**, 23-28 (2018).
2.	Y. N. Xia, G. M. Whitesides, Soft lithography. *Annu Rev Mater Sci* **28**, 153-184 (1998).
3.	V. Saggiomo, A. H. Velders, Simple 3D Printed Scaffold-Removal Method for the Fabrication of Intricate Microfluidic Devices. *Adv Sci* **2**, 1500125 (2015).
4.	T. O. Tasci, P. S. Herson, K. B. Neeves, D. W. M. Marr, Surface-enabled propulsion and control of colloidal microwheels. *Nat Commun* **7**, 10225 (2016).
5.	T. O. Tasci *et al.*, Enhanced Fibrinolysis with Magnetically Powered Colloidal Microwheels. *Small* **13** 1700954 (2017).
6.	T. Yang *et al.*, Microwheels on Microroads: Enhanced Translation on Topographic Surfaces. *Science Robotics* **4**, eaaw9525 (2019).
7.	X. J. A. Janssen, A. J. Schellekens, K. van Ommering, L. J. van Ijzendoorn, M. W. J. Prins, Controlled torque on superparamagnetic beads for functional biosensors. *Biosens Bioelectron* **24**, 1937-1941 (2009).
8.	C. Goubault *et al.*, Flexible magnetic filaments as micromechanical sensors. *Phys Rev Lett* **91**, 260802 (2003).
9.	B. Sprinkle, E. B. van der Wee, Y. Luo, M. Driscoll, A. Donev, Active dynamics in dense suspensions of microrollers. *arXiv preprint arXiv:2005.06002* (2020).
10.	J. W. Swan, J. F. Brady, Simulation of hydrodynamically interacting particles near a no-slip boundary. *Phys Fluids* **19**, 113306 (2007).
11.	J. F. Brady, R. J. Phillips, J. C. Lester, G. Bossis, Dynamic Simulation of Hydrodynamically Interacting Suspensions. *J Fluid Mech* **195**, 257-280 (1988).
12.	A. Sierou, J. F. Brady, Accelerated Stokesian Dynamics simulations. *J Fluid Mech* **448**, 115-146 (2001).
13.	B. Sprinkle, F. B. Usabiaga, N. A. Patankar, A. Donev, Large scale Brownian dynamics of confined suspensions of rigid particles. *J Chem Phys* **147**, 244103 (2017).
14.	S. Lim, A. Ferent, X. S. Wang, C. S. Peskin, Dynamics of a Closed Rod with Twist and Bend in Fluid. *Siam J Sci Comput* **31**, 273-302 (2008).
15.	S. D. Olson, S. Lim, R. Cortez, Modeling the dynamics of an elastic rod with intrinsic curvature and twist using a regularized Stokes formulation. *J Comput Phys* **238**, 169-187 (2013).
16.	S. Delong, F. B. Usabiaga, A. Donev, Brownian dynamics of confined rigid bodies. *J Chem Phys* **143** 144107 (2015).

17. S. F. Schoeller, A. K. Townsend, T. A. Westwood, E. E. Keaveny, Methods for suspensions of passive and active filaments. *arXiv preprint arXiv:1903.12609* (2019).
18. S. Kuei, B. Garza, S. L. Biswal, From strings to coils: Rotational dynamics of DNA-linked colloidal chains. *Phys Rev Fluids* **2**, 104102 (2017).
19. H. Jensenius, G. Zocchi, Measuring the spring constant of a single polymer chain. *Phys Rev Lett* **79**, 5030-5033 (1997).
20. N. Ziebacz, S. A. Wieczorek, T. Kalwarczyk, M. Fiakowski, R. Holyst, Crossover regime for the diffusion of nanoparticles in polyethylene glycol solutions: influence of the depletion layer. *Soft Matter* **7**, 7181-7186 (2011).